Journal of Materials Chemistry A

Thermal Properties and Lattice Anharmonicity of Li-ion Conducting Garnet Solid Electrolyte $Li_{6.5}La_3Zr_{1.5}Ta_{0.5}O_{12}$

Journal:	*Journal of Materials Chemistry A*
Manuscript ID	TA-ART-04-2024-002264.R1
Article Type:	Paper
Date Submitted by the Author:	04-Jun-2024
Complete List of Authors:	Wang, Yitian; University of California Riverside, Electric and computer engineering Li, Shuchen; University of California Riverside, Department of Electrical and Computer Engineering Wu, Nan; University of Texas at Austin, Mechanical Engineering Jia, Qianru; University of Texas at Austin, Mechanical Engineering Hoke, Thomas; University of California Riverside Shi, Li; University of Texas at Austin, Mechanical Engineering Li, Yutao; University of Texas at Austin, Mechanical Engineering Chen, Xi; University of California Riverside,

Thermal Properties and Lattice Anharmonicity of Li-ion Conducting Garnet Solid Electrolyte $Li_{6.5}La_3Zr_{1.5}Ta_{0.5}O_{12}$

Yitian Wang,[a,#] Shuchen Li,[a,#] Nan Wu,[b] Qianru Jia,[b] Thomas Hoke,[a] Li Shi,[b] Yutao Li[b,*,†] and Xi Chen[a*]

[a] Department of Electrical and Computer Engineering, University of California, Riverside, California, 92521, United States. Email: xichen@ucr.edu.

[b] Walker Department of Mechanical Engineering, The University of Texas at Austin, Austin, Texas, 78712, United States. Email: lytthu@utexas.edu

[†] Present address: Beijing Frontier Research Center on Clean Energy, Huairou Division, Institute of Physics, Chinese Academy of Sciences, Yongle North Second Street, Yanqi Economic Development Zone, Huairou District, 101400 Beijing, P. R. China.

[#] Contributed equally.

Abstract:

Garnet-type sold electrolytes have garnered significant interest for all-solid-state battery applications due to their high Li-ion conductivity and excellent compatibility with the metallic lithium anode. Although their ionic conductivity optimization and conduction mechanisms have been extensively studied, the thermal properties of garnet electrolytes remain poorly understood. The thermal conductivity, thermal expansion coefficient, and specific heat of solid electrolytes play a crucial role in determining the overall performance, safety, and reliability of battery devices. Understanding these properties is essential for enhanced thermal management and improved energy efficiency of batteries. Here, we investigate the thermal properties of Ta^{5+}-doped garnet $Li_{6.5}La_3Zr_{1.5}Ta_{0.5}O_{12}$ (LLZTO) polycrystals. The thermal conductivity measurement reveals a low-temperature peak at around 50 K. Above this temperature, the thermal conductivity shows a weak temperature dependence and approaches the calculated minimum thermal conductivity. The average phonon mean free path increases as the temperature decreases, reaching approximately 500 nm at 5 K. The linear thermal expansion coefficient obtained through the x-ray diffraction measurements is $1.71 \pm 0.01 \times 10^{-5}$ K^{-1} at 323 K, larger than the reported value for undoped $Li_7La_3Zr_2O_{12}$. The Grüneisen parameter of LLZTO calculated using measured thermal expansion coefficient and specific heat is 1.63 ± 0.04 at 300 K, indicating relatively strong phonon anharmonicity. Furthermore, the thermal conductivity of aged LLZTO is increased by 70%-80% at 300 K compared to the pristine samples, which can be attributed to the formation of Li_2CO_3 with increased thermal conductivity or reduced thermal boundary resistance. Our results provide useful insights into the structure-thermal property relationships that are closely relevant to thermal management of battery systems based on garnet solid electrolytes.

1. Introduction

In recent years, the quest for sustainable and high-performance energy storage and conversion technologies has intensified, driven by the imperative to address global energy challenges and mitigate environmental concerns. Among the important components of these advanced systems, solid electrolytes have emerged as promising candidates due to their potential to overcome the limitations associated with conventional organic electrolytes, such as flammability, leakage, and compatibility with electrodes.[1-3] Solid electrolytes, characterized by their robustness, stability, and ability to operate over a wide range of

temperatures, hold great promise for various applications, including solid-state batteries, electrochemical supercapacitors, and high-temperature fuel cells.[4-6]

The successful implementation of the energy storage and conversion technologies hinges not only on their electrochemical performance but also on their thermal properties, particularly thermal conductivity (κ) and thermal expansion coefficient.[7-10] The thermal properties of solid electrolytes play a crucial role in determining the safety and reliability of energy storage and conversion devices.[11] Lithium plating, which leads to reduced capacity in lithium-ion batteries, is sensitive to temperature. Therefore, temperature control becomes particularly important as it allows for the regulation of internal temperature distributions, thereby enhancing the uniformity of lithium deposition and mitigating the formation of dendrites.[12] Efficient thermal management is essential for maintaining the operational stability and longevity of energy storage and conversion devices.[13] The temperature profile of a battery depends on the thermal conductivity of its component. In particular, the thermal conductivity of solid electrolytes is crucial for determining the overall thermal resistance of the cell, especially if their thermal conductivity is low. Furthermore, thermal expansion coefficient is a critical property that controls the mechanical integrity and structural stability of solid electrolytes, especially during thermal cycling.[14] Understanding the relationship between thermal expansion coefficient and temperature variation is essential for designing durable and long-lasting energy storage and conversion devices.

The garnet solid electrolyte with the nominal formula $Li_7La_3Zr_2O_{12}$ (LLZO) shows great promise as a solid electrolyte for all-solid-state batteries owing to its good lithium ionic conductivity exceeding 10^{-4} S cm^{-1} at room temperature and its stability when paired with electrode materials.[15-19] In particular, Ta-doped LLZO with composition $Li_{6.5}La_3Zr_{1.5}Ta_{0.5}O_{12}$ (LLZTO) shows a remarkable room-temperature ionic conductivity of 10^{-3} S cm^{-1}.[20] Despite many studies on understanding and improving its ionic properties,[21-23] thermal properties of LLZO remain elusive. Recently, Cheng *et al.*[24] measured the specific heat (C_p) and thermal conductivity of $Li_{6.4}La_3Zr_{1.4}Ta_{0.6}O_{12}$ from 150 to 500 K, and observed a low κ of 1.4 W m^{-1} K^{-1} at room temperature, which approaches the calculated minimum value. Neises *et al.*[25] studied the thermal conductivity of Ta^{5+}- and Al^{3+}-doped LLZO with different grain sizes from 300 to 1225 K, and observed that thermal transport is independent of grain size. However, the low-temperature thermal transport in LLZTO, such as the peak thermal conductivity, has not been studied so far. At elevated temperatures, thermal conductivity decreases with increasing temperature due to enhanced phonon-phonon scattering. Conversely, at lower temperatures, thermal conductivity declines with decreasing temperature due to reduced phonon specific heat and weak phonon-phonon scattering compared to extrinsic scattering processes. As a result, a peak in the lattice thermal conductivity emerges well below room temperature in typical crystals. The measurement of this peak can offer valuable insights into the interplay between intrinsic phonon-phonon and extrinsic phonon scattering processes by defects and boundaries.[26]

Along with thermal conductivity, the thermal expansion coefficient and Grüneisen parameter (γ) are two other important properties that contribute to fundamental understanding of lattice anharmonicity and are critical for thermomechanical reliability of batteries. A prior study has reported the linear thermal expansion coefficient (α_l) of LLZO and the effect of Al doping content.[27] However, the thermal expansion coefficient of LLZTO has not been reported. Furthermore, Grüneisen parameter describes how the vibrational properties of a material change in response to changes in volume or pressure. This parameter is an important descriptor for phonon anharmonicity in a material.[28] It is noted that the Grüneisen parameter of LLZTO has not been determined experimentally.

Previous studies have found that garnet LLZO is unstable in the presence of moisture.[29-32] Both experimental and theoretical work[33, 34] indicate that garnet exposed to H_2O and CO_2 forms a Li-ion insulating $LiOH/Li_2CO_3$ surface layer. As a result, the ionic conductivity of LLZO can be reduced in aged

samples due to the increased interfacial resistance and the reduction of Li ions in bulk LLZO.[35, 36] However, the effect of impurities on the thermal transport in garnet electrolytes is still unknown, which is crucial for effective thermal management of aged battery cells.

Here, we study the thermal properties and lattice anharmonicity of LLZTO polycrystals. The thermal conductivity of LLZTO is measured in a large temperature range of 5-824 K. The obtained thermal conductivity exhibits a peak at about 50 K and a weak temperature dependence above 200 K. The average phonon mean free path is calculated from the obtained thermal conductivity and reaches about 500 nm at low temperatures. The linear thermal expansion coefficient (α_l) of LLZTO from 323 K to 523 K is determined by high-temperature x-ray diffraction (XRD) measurements. Together with the reported bulk modulus,[37] the measured thermal expansion coefficient and specific heat data are used to obtain the Grüneisen parameter as 1.63 ± 0.04 at 300 K, suggesting relatively large anharmonicity in LLZTO. Furthermore, the aged LLZTO samples exhibit an enhanced thermal conductivity compared to the pristine samples. This finding can be attributed to the formation of Li_2CO_3 impurities.

2. Experimental

2.1 Materials synthesis

The starting material was a mixture of 50 mol% Li_2CO_3 (Thermo Fisher Scientific, 99%), 23 mol% La_2O_3 (Sigma-Aldrich, 99.99%), 23 mol% ZrO_2 (Sigma-Aldrich, 99%) and 4 mol% Ta_2O_5 (Thermo Fisher Scientific, 99%), corresponding to the formula of $Li_{6.5}La_3Zr_{1.5}Ta_{0.5}O_{12}$ with 20% excess of Li_2CO_3. The mixture was fired in air at 1123 K for 60 hours. The obtained LLZTO powders were then cold pressed into a pellet under 300 MPa and sintered in LLZTO bed powder at 1173 K for 8 hours, designated as Sample #1. In addition, a polycrystalline LLZTO sample was prepared by spark plasma sintering under 50 MPa in vacuum at 1373 K for 15 min, designated as Sample #2. To study the thermal conductivity of Li_2CO_3, a pellet was prepared by cold pressing followed by sintering in air at 873 K for 6 hours.

2.2 Phase and structure characterization

The purity and crystal structure of the samples were characterized by powder XRD with a Cu Kα source (λ = 1.54 Å). Rietveld refinement was performed to calculate the lattice parameters. The morphology of the samples was observed by a TESCAN Vega3 SBH scanning electron microscope (SEM) equipped with energy dispersive x-ray spectrometry (EDS). Raman measurement was performed to study the impurities in the aged samples using the Horiba LabRam with a 532 nm Coherent Sapphire laser at room temperature.

2.3 Thermal property measurements

The density (ρ) of the samples were measured using the Archimedes' method. The specific heat of the sample from 2 to 276 K was measured with a Quantum Design Physical Property Measurement System (PPMS). The high-temperature specific heat data were collected using a Netzsch 404 differential scanning calorimeter (DSC) with a sapphire standard. The PPMS was employed to measure the thermal conductivity along the direction perpendicular to the cold-pressing direction from 5 to 300 K. The high-temperature thermal diffusivity (α) was measured by using the laser flash diffusivity method in a Netzsch Laser Flash Apparatus (LFA) 457 instrument. The thermal conductivity in the temperature range of 300-824 K was calculated with $\kappa = \rho\alpha C_p$. Thermogravimetric analysis (TGA) was used to measure weight changes of LLZTO polycrystals from 300 to 1272 K under N_2 gas flow using Netzsch TG 209 F1 Libra.

3. Results and discussion

3.1 Phase and microstructure

Fig. 1(a) illustrates the crystal structure of LLZTO. Two types of lithium sites form a network in the frame built by octahedral Zr/Ta-O_6 and dodecahedral La-O_8. The XRD pattern of LLZTO is displayed in Fig. 1(b). The main phase can be indexed based on a previously reported cubic structure with space group $Ia\bar{3}d$.[38] No impurities have been observed. Rietveld refinement was performed to determine a lattice constant of 12.918(3) Å, comparable with the previously reported value of 12.921 Å.[39] To investigate the microstructures, we performed the SEM studies on a LLZTO polycrystal prepared by cold pressing. The average grain size is found to be about 8 μm, as shown in Fig. 1(c). The grain size distribution can be found in Fig. S1 Electronic Supplementary Information (ESI). The EDS mapping results for the sample are illustrated in Fig. 1(d). La, Zr and Ta elements show a uniform distribution, which indicates a homogeneous distribution of dopants in the cold-pressed sample. The EDS analysis confirms that the atomic ratio of La:Zr:Ta is close to the designed ratio of 3.0:1.5:0.5.

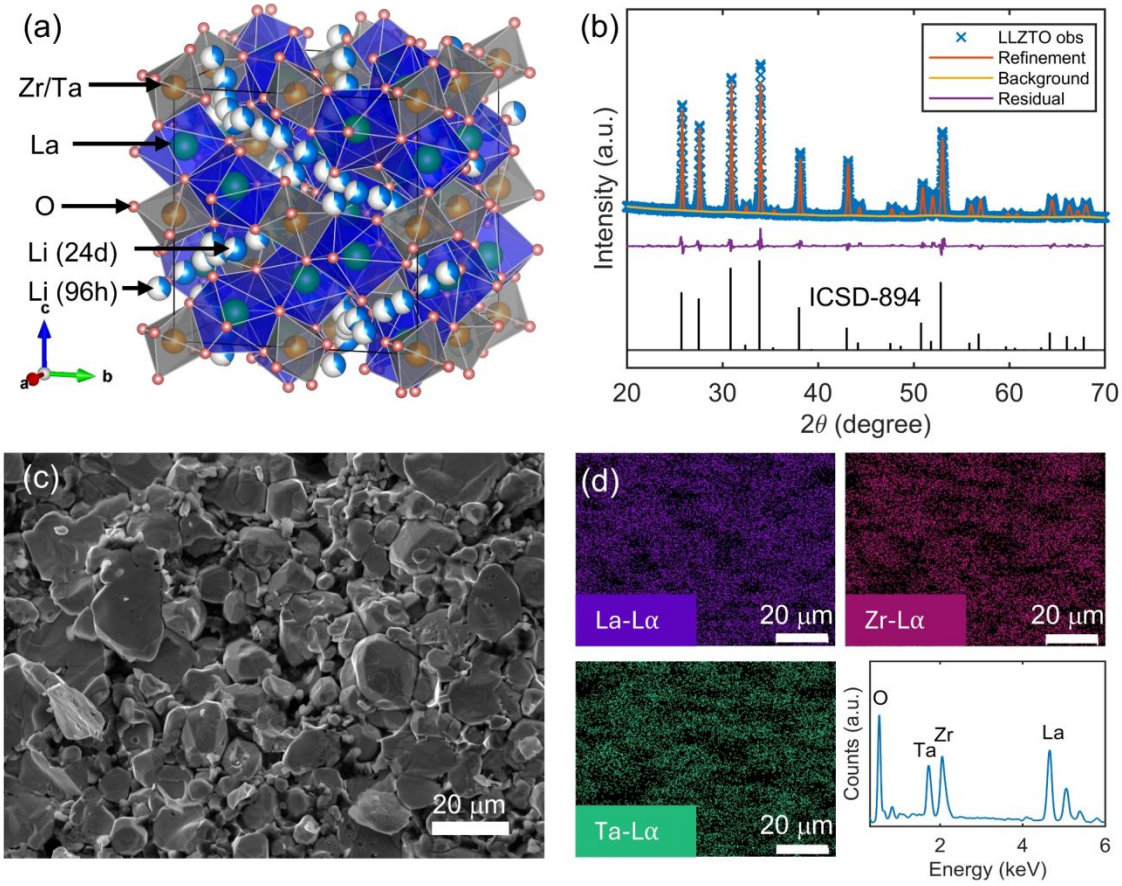

Fig. 1 (a) Crystal structure of cubic LLZTO. (b) Rietveld refinement of XRD result for LLZTO powders prepared by solid-state reaction. The reliability parameter of R_{wp} is 7.94%. (c) SEM image and (d) EDS analysis of the fracture surface of the LLZTO pellet prepared by cold pressing.

3.2 Thermal property measurements and analysis

As shown in Fig. 2(a), the specific heat of LLZTO was measured by the PPMS from 2 to 276 K and DSC from 308 to 964 K. Both sets of measurement results exhibit a consistent and continuous trend. No first

order phase transition is observed within the measured temperature range. This is consistent with previous studies[40, 41] showing that sufficient Ta-doping in LLZO can stabilize the cubic phase at room temperature and prevent tetragonal-to-cubic phase transition. The specific heat and other room-temperature physical properties of LLZTO are summarized in Table 1. The specific heat at low temperatures can be fitted to the Debye model using

$$C_p(T) = \frac{12\pi^4 k_B}{5\rho}\left(\frac{N}{V}\right)\left(\frac{T}{\theta_D}\right)^3 + bT, \quad (1)$$

where T is temperature, k_B is the Boltzmann constant, θ_D is the Debye temperature, and b is the coefficient of electronic contribution to specific heat. The atomic density of the system (N/V) is estimated as 8.7×10^{28} m^{-3} and ρ is the theoretical density of 5428 kg m^{-3} determined from the XRD refinement. The fitting yields a Debye temperature of 479 K, close to the previously reported value of 526 K for $Li_{6.45}Al_{0.05}La_3Zr_{1.6}Ta_{0.4}O_{12}$.[25] The bulk sound velocity (v_b) is related to the Debye temperature (θ_D) as

$$\left(\frac{k_B}{\hbar}\right)^3 \theta_D^3 = \frac{6\pi^2 N}{V} v_b^3. \quad (2)$$

The corresponding bulk sound velocity v_b is calculated as 3627 m s^{-1}, which agrees reasonably well with the previously reported result of 3953 m s^{-1} for $Li_{6.45}Al_{0.05}La_3Zr_{1.6}Ta_{0.4}O_{12}$[25] calculated based on measured mechanical properties.[37]

The measured thermal conductivity of the cold-pressed LLZTO is shown in Fig. 2(b). It has been found that thermal conductivity exhibits a peak at about 50 K. Above 200 K, the thermal conductivity shows a weak temperature dependence. The obtained value at 300 K is 1.2 ± 0.2 W m^{-1} K^{-1}, which is consistent with the reported data for $Li_{6.4}La_3Zr_{1.4}Ta_{0.6}O_{12}$[24] and $Li_{6.45}Al_{0.05}La_3Zr_{1.6}Ta_{0.4}O_{12}$.[25] The slightly smaller value of our sample can be resulted from its porosity. This finding suggests that the thermal conductivity of LLZO is nearly independent of chemical substitution. It is noticed that the temperature dependence of thermal conductivity for our sample is different from the measured data for $Li_{6.4}La_3Zr_{1.4}Ta_{0.6}O_{12}$, which exhibits a decrease of thermal conductivity with reduced temperature below 300 K.[24] This discrepancy can be attributed to the different growth methods used for the two samples, which may result in varying defect concentrations and grain sizes. The decrease in thermal conductivity with decreasing temperature is commonly observed in disordered materials exhibiting high defect concentrations, or materials with small grain sizes.[42, 43]

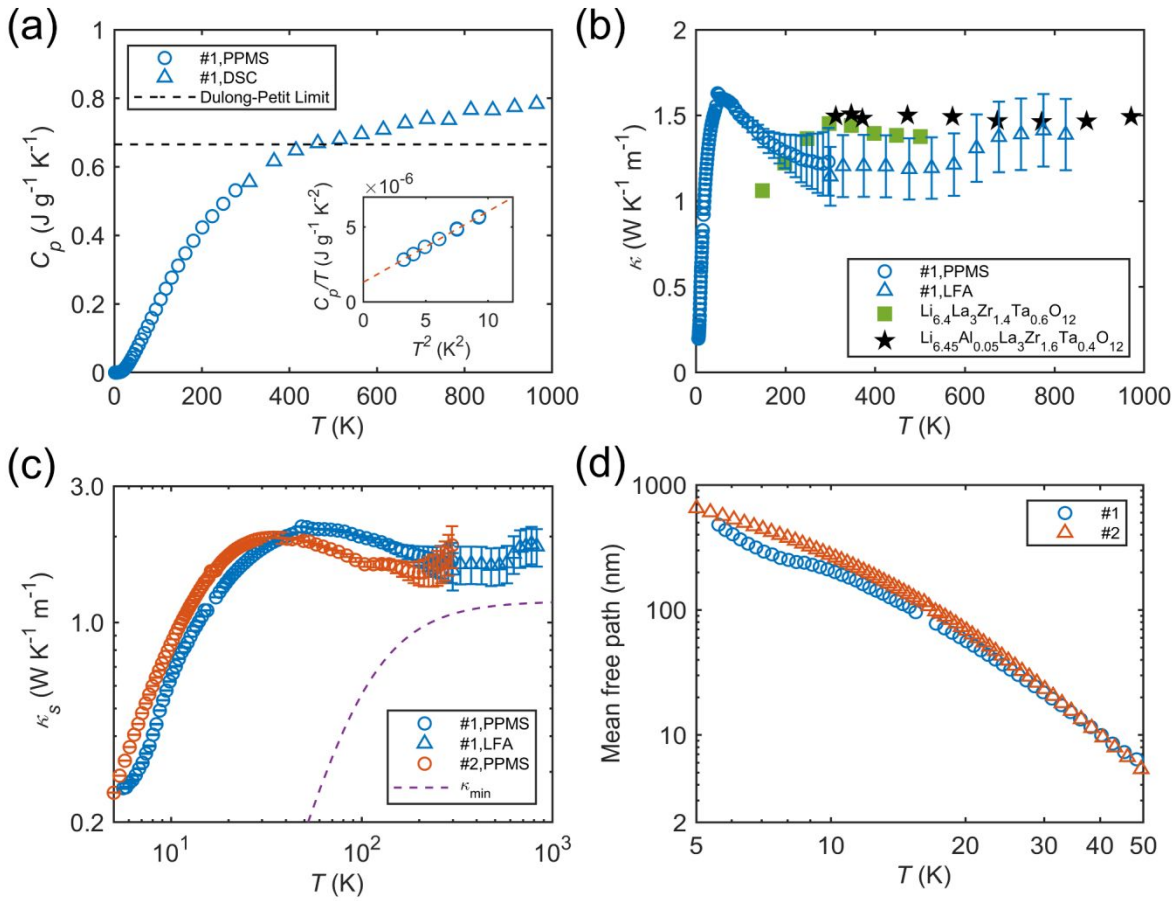

Fig. 2 (a) Specific heat of LLZTO measured by the PPMS and DSC. The inset shows the C_p/T versus T^2 at low temperatures. (b) Thermal conductivity of cold-pressed LLZTO (#1) measured by the PPMS and LFA. The reported experimental data for $Li_{6.4}La_3Zr_{1.4}Ta_{0.6}O_{12}$[24] and $Li_{6.45}Al_{0.05}La_3Zr_{1.6}Ta_{0.4}O_{12}$[25] are included for comparison. (c) Solid thermal conductivity of the LLZTO samples prepared by cold-pressing (#1) and spark plasma sintering (#2), respectively. The dashed line is the calculated minimum thermal conductivity. (d) Calculated phonon mean free path of LLZTO at low temperatures.

Table 1. Room-temperature physical properties of LLZTO polycrystals

Sample	κ (w m^{-1} K^{-1})	κ_s (w m^{-1} K^{-1})	C_p (J g^{-1} K^{-1})	θ_D (K)	v_b (km s^{-1})	α_l (10^{-5} K^{-1})	γ
LLZTO	1.2 ± 0.2	1.6 ± 0.3	0.55 ± 0.01	479 ± 1	3.63 ± 0.01	1.59 ± 0.01	1.63 ± 0.04

To correct the porosity effect, the solid thermal conductivity (κ_s) can be calculated using the Maxwell-Eucken relation as[44-47]

$$\kappa_S = \kappa \frac{\kappa_p + 2\kappa_s - \Phi(\kappa_p - \kappa_s)}{\kappa_p + 2\kappa_s + 2\Phi(\kappa_p - \kappa_s)}, \quad (3)$$

where κ_p is the pore thermal conductivity, and Φ is the porosity, which is found to be 18% for the cold-pressed LLZTO pellet. κ_p is equal to 0 as our measurements were conducted under ultra-high vacuum. The obtained κ_s is presented in Fig. 2(c) together with the data for a sample prepared by spark plasma sintering. We further evaluated the minimum thermal conductivity (κ_{min}) of LLZTO using the model developed by Cahill *et al*.[48]

$$\kappa_{min} = \left(\frac{\pi}{6}\right)^{1/3} k_B \left(\frac{N}{V}\right)^{2/3} 3v_b \left(\frac{T}{\theta_D}\right)^2 \int_0^{\theta_D/T} \frac{x^3 e^x}{(e^x-1)^2} dx. \quad (4)$$

This equation is formulated upon the Einstein model to compute the minimum lattice thermal conductivity of highly disordered solids. In this model, thermal transport is characterized by the random walk of energy among localized oscillators with varying frequencies, with the primary energy transfer occurring between nearest neighbors. The calculated κ_{min} for LLZTO is 1.07 W m^{-1} K^{-1} at 300 K. The obtained κ_s approaches the calculated κ_{min}, suggesting the phonon mean free path in LLZTO is at the same order of atomic spacing at high temperatures.

At temperatures significantly lower than θ_D, thermal transport is predominantly governed by acoustic phonons. For this low-temperature limit, we calculated the phonon mean free path (L) using the Debye model[49] given by

$$L = \kappa_s \left[\left(\frac{k_B^4 T^3}{2\pi^2 v_b^2 \hbar^3} \right) \int_0^{\theta_D/T} \frac{x^4 e^x dx}{(e^x-1)^2} \right]^{-1}. \quad (5)$$

The obtained phonon mean free path data from 5 K to 50 K are plotted in Fig. 2(b). The phonon mean free path of LLZTO approaches about 500 nm at low temperatures, which is smaller than the measured average grain size of 8 μm. This finding suggests that phonon scattering at grain boundaries may not significant, with the primary scattering occurring at inhomogeneities or defects within the crystal lattice, which is consistent with a previous study.[25] The phonon mean free path decreases with increasing temperature due to the increased phonon-defect scattering and reaches a value of about 5 nm around 50 K.

3.3 High temperature XRD, thermal expansion coefficient and Grüneisen parameter

To study the phonon anharmonicity of LLZTO, we performed high-temperature XRD measurements from 323 to 523 K, as shown in Fig. 3. The sample is stable up to 523 K since no phase transition was observed. The lattice constant a of LLZTO is calculated using the Bragg's law, as shown in Fig. 4(a) together with the reported lattice constant of $Li_6La_3ZrTaO_{12}$ and LLZO obtained by XRD analysis.[27, 50] The a value of LLZTO increases monotonically with temperature. We note that the a value for LLZTO lies between the data reported for $Li_6La_3ZrTaO_{12}$ and LLZO.[27, 50] The temperature dependence of a can be fitted by a second-order polynomial as[51]

$$a(T) = a_0 + a_1 T + a_2 T^2, \quad (6)$$

where a_0, a_1 and a_2 are fitting parameters. The obtained fitting results are a_0 = 12.90 Å, a_1 = 5.814×10^{-6} Å K^{-1}, and a_2 = 3.327×10^{-7} Å K^{-2}.

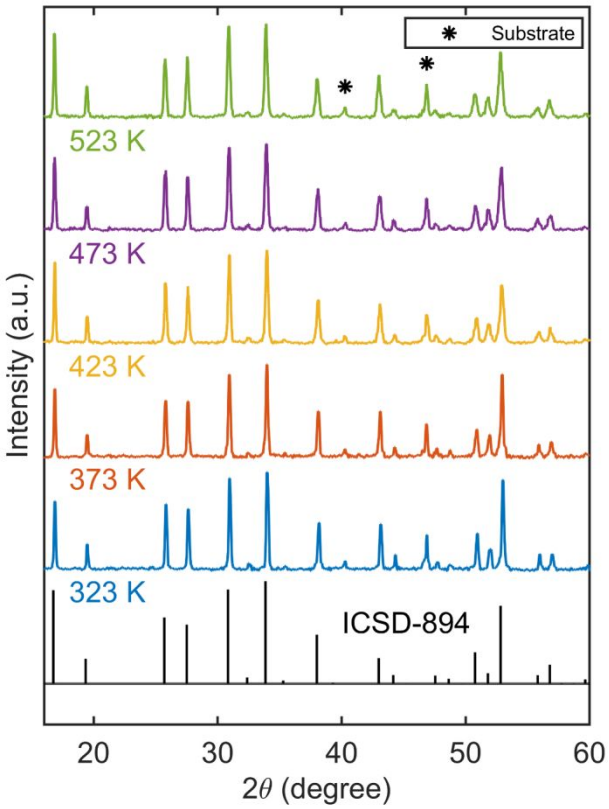

Fig. 3 XRD patterns of LLZTO from 323 to 523 K.

According to the definition of the linear thermal expansion coefficient α_l, $\alpha_l \equiv \frac{1}{a}\frac{da}{dT}$, temperature dependence of the thermal expansion coefficient can be calculated as

$$\alpha_l(T) = (a_1 + 2a_2T)/(a_0 + a_1T + a_2T^2). \quad (7)$$

The obtained α_l of LLZTO increases nearly linearly with temperature from 1.71 ± 0.01 × 10^{-5} K^{-1} at 323 K to 2.72 ± 0.01 × 10^{-5} K^{-1} at 523 K, as shown in Fig. 4(b). The α_l data of $Li_6La_3ZrTaO_{12}$ and LLZO are also calculated with the same method using the reported lattice constants and are plotted as solid lines in Fig. 4(b). The α_l of LLZTO near 300 K is similar to the result for $Li_6La_3ZrTaO_{12}$ while the reported α_l of LLZO is 18% smaller. Furthermore, our LLZTO sample demonstrates a similar temperature dependence of α_l as $Li_6La_3ZrTaO_{12}$, while the α_l of LLZO has a much weaker temperature dependence. Compared to other garnets,[52] LLZTO exhibits a thermal expansion coefficient approximately twice as large. The volumetric thermal expansion coefficient (α_v) of LLZTO with a cubic crystal structure can be estimated as $\alpha_v = 3\alpha_l$, which leads to a value of 4.77 ± 0.03 × 10^{-5} K^{-1} at 300 K.

One method to assess phonon anharmonicity is by calculating the Grüneisen parameter using the following equation[53]

$$\gamma = \frac{\alpha_V B_S}{C_V \rho}, \quad (8)$$

where B_S is the adiabatic bulk moduli, and C_v is the specific heat at constant volume. The α_v of 4.77 ± 0.03 $\times 10^{-5}$ K^{-1} is determined from the high-temperature XRD study. The adiabatic bulk modulus was reported as 96.0 ± 1.4 GPa for LLZO.[37] The specific heat measured in this work is 0.55 J g^{-1} K^{-1} at 300 K. Using the relationship[54] between C_v and C_p and reported compressibility of LLZO,[55] the C_v of LLZTO is calculated as 0.52 ± 0.01 J g^{-1} K^{-1}. We use the theoretical density of LLZTO, 5.428 g cm^{-3}, determined from the XRD refinement. Therefore, the calculated Grüneisen parameter is 1.63 ± 0.04, which is close to the reported Grüneisen parameter of 1.56-1.65 for Nb-doped LLZO.[56] Compared to γ = 0.77 for Cu_2Se[57] and γ =1.2 for $Li_{10}GeP_2S_{12}$,[58] the Grüneisen parameter of LLZTO indicates a relatively strong anharmonicity of phonons. It has been found that some superionic conductors also exhibit low thermal conductivity, which is attributed to large phonon anharmonicity.[59, 60] In order to better understand the phonon properties in LLZTO, further research is required to investigate its phonon band structures.

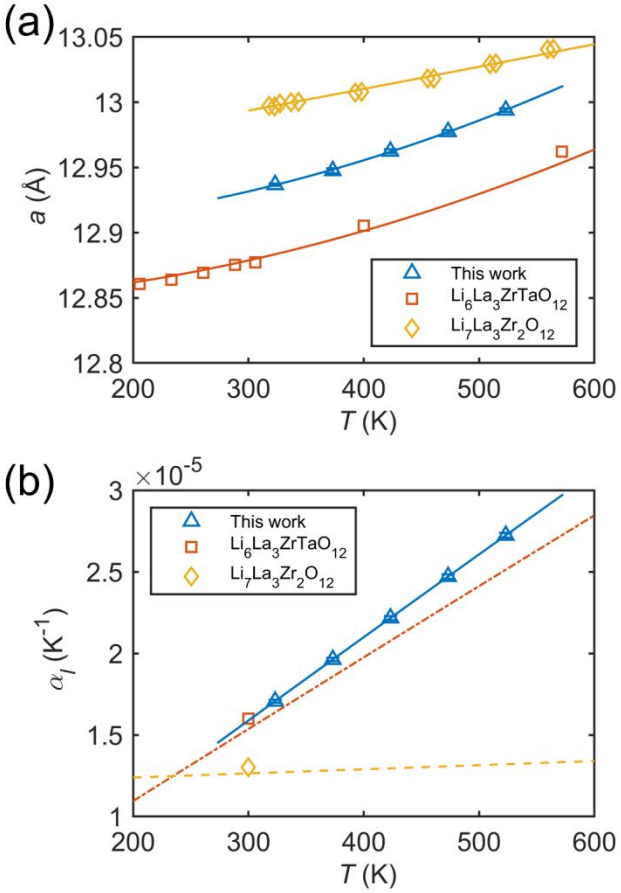

Fig. 4 (a) Lattice constant of LLZTO as a function of temperature. Shown for comparison are the reported data of $Li_6La_3ZrTaO_{12}$[50] and $Li_7La_3Zr_2O_{12}$[27]. The lines represent the fitting achieved using Equation (6). (b) Linear thermal expansion coefficient calculated using Equation (7) and compared with the data reported for $Li_6La_3ZrTaO_{12}$[50] and $Li_7La_3Zr_2O_{12}$[27]. The lines represent the calculated thermal expansion coefficient by analyzing the reported lattice constants using Equations (6) and (7).

3.4 Effect of aging on thermal conductivity

LLZTO is chemically unstable against moisture. Li ions in LLZTO can be exchanged with protons under ambient air humidity.[61] The detailed reactions are given as follows:[62]

$$Li_{6.5}La_3Zr_{1.5}Ta_{0.5}O_{12} + x\ H_2O \rightarrow Li_{6.5-x}H_xLa_3Zr_{1.5}Ta_{0.5}O_{12} + x\ LiOH, \quad (9)$$

$$2LiOH + CO_2 \rightarrow Li_2CO_3 + H_2O. \quad (10)$$

The XRD pattern of a LLZTO sample aged in air for approximately one year is depicted in Fig. 5(a), from which it can be seen that Li_2CO_3 is formed in the sample. Fig. 5(b) shows the Raman spectrum of the aged LLZTO sample. All Raman peaks below 800 cm^{-1} are associated with LLZTO, while the Raman peak at 1090 cm^{-1} can be attributed to the presence of Li_2CO_3, as reported in previous studies.[63, 64] It is noted that the Raman peak is very sharp for Li_2CO_3, while the peaks are much broader for LLZTO. The peak width in the Raman spectrum is related to the crystallinity of the material being analyzed. When a material is crystalline, its atoms are arranged in a regular, repeating pattern, resulting in sharp and well-defined peaks in the Raman spectrum. This is because the vibrational modes of the material are restricted to specific frequencies dictated by the crystalline lattice structure. On the other hand, in an amorphous or disordered material, the lack of long-range order leads to broad peaks in the Raman spectrum. Our Raman study indicates that Li_2CO_3 has better crystallinity than LLZTO.

We further studied the microstructures of the aged sample using SEM, as shown in Fig. 5(c-d). The grain size shows a large distribution, ranging from about 2 to 40 μm. Some rough layers are formed on the surface of some grains, indicating that the grain surface of LLZTO reacted with moisture, as reported in previous studies.[65, 66] Some grains show large cracks, which can be caused by the volume change due to the reaction with moisture. Additional SEM images of cracked grains can be found in Fig. S2 (ESI). EDS analysis reveals that the cracked grains exhibit a deficiency in Ta and Zr. As shown in Fig. 5(e), the cracked grain has a La:Zr:Ta ratio of 3.0:0.03:0.01 while the grain without crack has a La:Zr:Ta ratio of 3.0:1.37:0.65. The EDS mapping results of the cracked grain region can be found in Fig. S3 (ESI). It has been reported that the reaction usually occurred at the surface of the grain, and the garnet structure was preserved.[65] However, our result suggests that the reaction can also occur within grains, leading to grain fracture.

TGA analysis was performed on one aged sample under N_2 gas flow, as displayed in Fig. 5 (f). At least three weight loss steps can be identified, similar to a prior study.[61] Among them, step Ⅰ is due to the evaporation of absorbed surface water at about 523 K, step Ⅱ is related to the release of H^+ as H_2O at around 673-723 K, and step Ⅲ can be attributed to the release of CO_2 in the temperature range of 823-973 K. Therefore, the weight loss from step Ⅱ can be used to quantify the percentage of Li^+/H^+ exchange in the LLZTO sample. The chemical composition of the aged sample is found to be $Li_{2.05}H_{4.45}La_3Zr_{1.5}Ta_{0.5}O_{12}$.

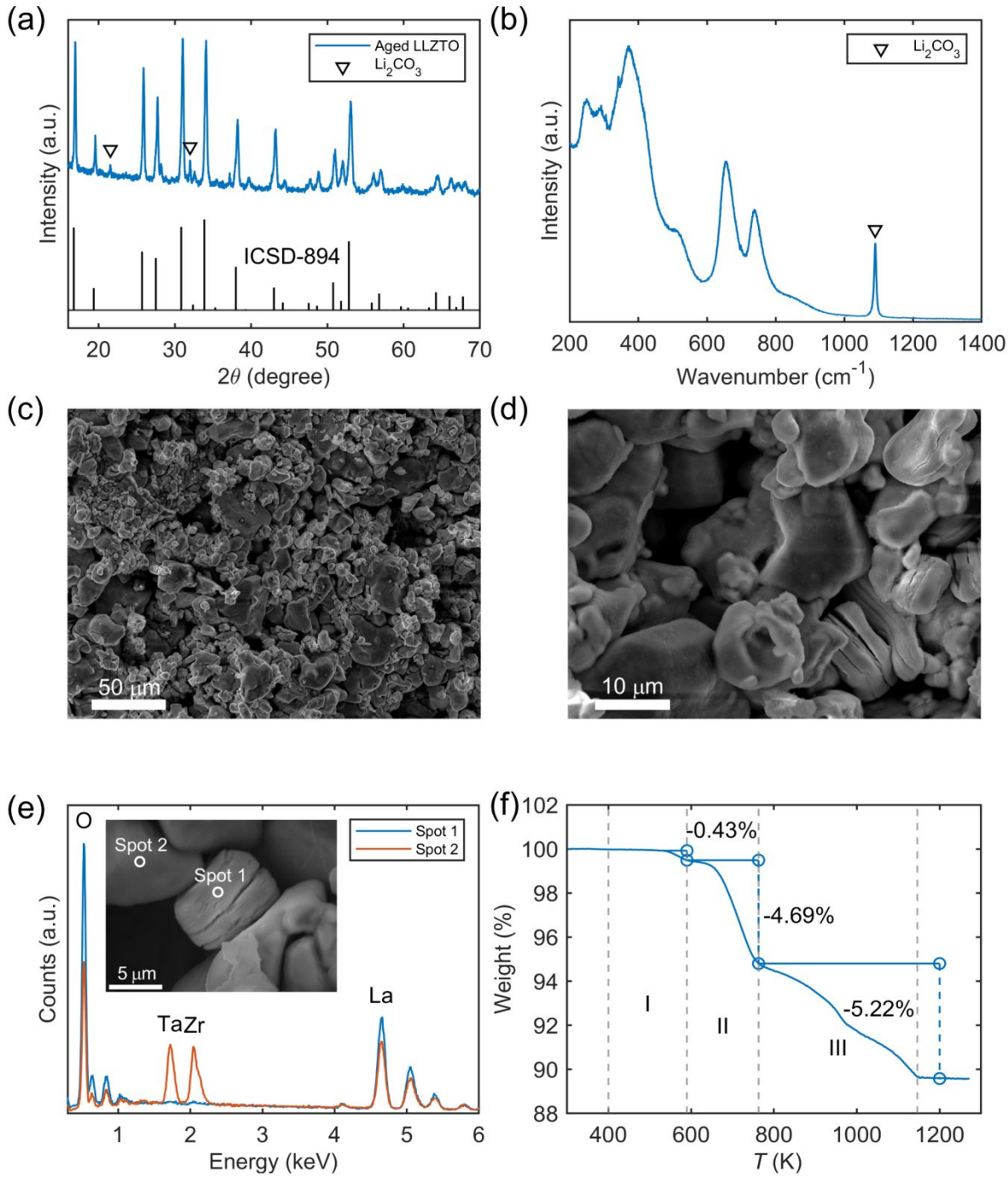

Fig. 5 (a) XRD pattern of the LLZTO aged in air for one year showing the presence of Li_2CO_3. (b) Raman spectrum of the aged sample. (c-d) SEM images of the aged sample showing the cracked grains with rough surfaces. (e) EDS results on selected region of the aged sample. (f) TGA analysis of the aged sample.

The thermal conductivity data of the aged samples are shown in Fig. 6. Interestingly, compared to the pristine samples, the aged samples exhibit enhanced thermal conductivity nearly in all measured

temperature range. The room-temperature thermal conductivity of the aged samples is increased by 70-80%. This finding seems to contradict the SEM observation. The formation of rough layers on the grain surface and cracks within grains are expected to increase the phonon scattering within grains and at gain boundaries, leading to a reduced thermal conductivity. Therefore, the increased thermal conductivity must be caused by another mechanism. We note that the aged samples contain a significant amount of Li_2CO_3, which can affect the thermal transport in the material. To verify this, we measured the thermal conductivity of a cold-pressed Li_2CO_3, as displayed in Fig. 6. Indeed, Li_2CO_3 exhibits a larger thermal conductivity in the temperature range of 20-300 K. The obtained room-temperature thermal conductivity of Li_2CO_3 is 2.5 W m^{-1} K^{-1}, twice as large as that of pristine LLZTO. Therefore, the increase thermal conductivity of the aged samples can be attributed to the presence of Li_2CO_3.

Another possible reason for the enhanced thermal conductivity could be the reduction in thermal boundary resistance in the aged samples. Thermal boundary resistance arises from phonon scattering at interfaces. When the resistance is reduced, phonon scattering is minimized, allowing phonons to propagate more freely across the boundary and thereby increasing phonon transmission coefficient and thermal conductivity. It has been found that Li_2CO_3 usually forms on the surface of garnet LLZO.[65] Owing to the high crystallinity nature of Li_2CO_3, the phonon transmission coefficient across boundaries could be enhanced. A similar observation has been found in other materials by inserting an interfacial layer.[67, 68] Therefore, we estimated the thermal boundary resistance in LLZTO samples using the model developed by Nan *et al.*[69] The detailed analysis can be found in the Supplementary Information. The obtained thermal boundary resistance values are 9.2×10^{-4} m^2 K W^{-1} and 5.5×10^{-4} m^2 K W^{-1} at 290 K for the pristine and aged sample #1, respectively. It can be seen that the thermal boundary resistance is significantly reduced in the aged sample.

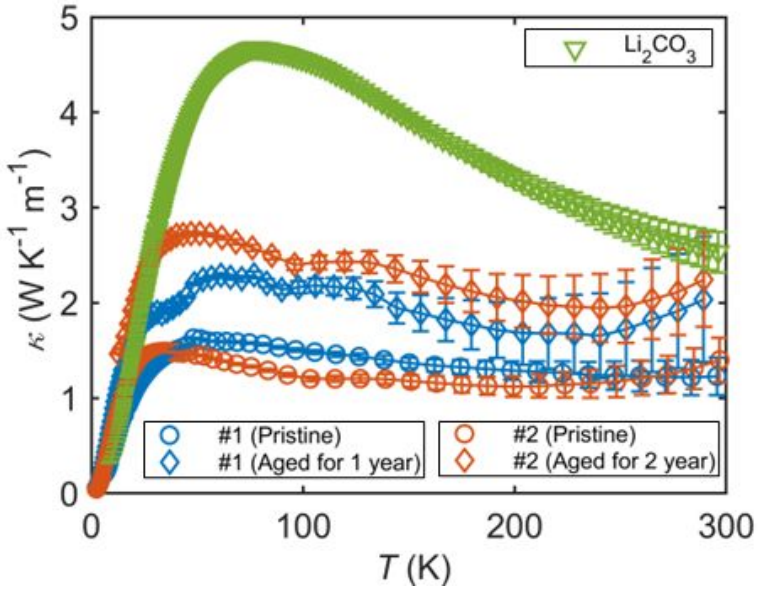

Fig. 6 Thermal conductivity of the aged LLZTO samples compared to the pristine samples. Shown for comparison is the thermal conductivity of a cold-pressed Li_2CO_3 sample. The thermal conductivity data of sample #1 (pristine) and #2 (pristine) are the same as the data plotted in Fig. 2.

4. Conclusions

We investigate the thermal properties and lattice anharmonicity of garnet solid electrolyte LLZTO. The thermal conductivity of polycrystalline LLZTO exhibits a peak at about 50 K, and a weak temperature dependence above 200 K. The measured room-temperature thermal conductivity is about 1.2 ± 0.2 W m^{-1} K^{-1}, which approaches the calculated minimum thermal conductivity. The calculated average phonon mean free path increases with decreasing temperature and reaches about 500 nm at 5 K. The measured linear thermal expansion coefficient is about 1.71 ± 0.01 × 10^{-5} K^{-1} at 323 K and increases with temperature. This thermal expansion coefficient is larger than the reported value for undoped $Li_7La_3Zr_2O_{12}$.[27] Together with the separately measured bulk modulus,[37] the specific heat and thermal expansion coefficient measured here allow us to determine a room-temperature value of 1.63 ± 0.04 for the Grüneisen parameter, indicating relatively large phonon anharmonicity in LLZTO. Furthermore, the aged samples show an enhanced thermal conductivity as compared to the pristine samples, which can be attributed to the presence of Li_2CO_3 with larger thermal conductivity than LLZTO. These findings offer useful insights into the relationships between structure and thermal properties in garnet-type solid electrolytes, which are crucial for effective thermal management in all-solid-state batteries.

Author contributions

Yitian Wang: investigation, validation, writing – original draft. Nan Wu: investigation, methodology, writing - review and editing. Shuchen Li: investigation, validation, writing- review and editing. Qianru Jia: investigation, writing- review and editing. Li Shi: investigation, writing- review and editing. Yutao Li: conceptualization, writing – review & editing, resources, supervision. Xi Chen: conceptualization, methodology, writing – review & editing, resources, funding acquisition, supervision.

Conflicts of interest

There are no conflicts to declare.

Acknowledgements

This work was supported by the National Science Foundation under Grant No. 2144328. Xi Chen and Yitian Wang acknowledge support from OASIS internal funding award from University of California, Riverside. The work at Austin is supported by National Science Foundation Thermal Transport Processes Program (Award No. 2321302).

References

1. J. B. Goodenough and Y. Kim, *Chemistry of Materials*, 2010, **22**, 587-603.
2. Q. Zhao, S. Stalin, C.-Z. Zhao and L. A. Archer, *Nature Reviews Materials*, 2020, **5**, 229-252.
3. A. Manthiram, X. Yu and S. Wang, *Nature Reviews Materials*, 2017, **2**, 16103.
4. F. Zheng, M. Kotobuki, S. Song, M. O. Lai and L. Lu, *Journal of Power Sources*, 2018, **389**, 198-213.
5. A. Nishino, *Journal of Power Sources*, 1996, **60**, 137-147.
6. J. W. Fergus, *Journal of Power Sources*, 2006, **162**, 30-40.

7. C.-W. Wu, X. Ren, W.-X. Zhou, G. Xie and G. Zhang, *APL Materials*, 2022, **10,** 040902.
8. M. Bertrand, S. Rousselot, D. Aymé-Perrot and M. Dollé, *Materials Advances*, 2021, **2**, 2989-2999.
9. Y. Cui, M. M. Mahmoud, M. Rohde, C. Ziebert and H. J. Seifert, *Solid State Ionics*, 2016, **289**, 125-132.
10. S. Yazdani, R. Kashfi-Sadabad, M. D. Morales-Acosta, R. D. Montaño, T. N. Vu, H. D. Tran, M. Zhou, Y. Liu, J. He and M. Thompson Pettes, *Applied Physics Letters*, 2020, **117,** 011903.
11. M. T. Agne, T. Böger, T. Bernges and W. G. Zeier, *PRX Energy*, 2022, **1**, 031002.
12. H. Ge, J. Huang, J. Zhang and Z. Li, *Journal of The Electrochemical Society*, 2016, **163**, A290.
13. J. Kim, J. Oh and H. Lee, *Applied Thermal Engineering*, 2019, **149**, 192-212.
14. H.-C. Yu, D. Taha, T. Thompson, N. J. Taylor, A. Drews, J. Sakamoto and K. Thornton, *Journal of Power Sources*, 2019, **440**, 227116.
15. R. Murugan, V. Thangadurai and W. Weppner, *Angewandte Chemie International Edition*, 2007, **46**, 7778-7781.
16. T. Krauskopf, H. Hartmann, W. G. Zeier and J. Janek, *ACS Applied Materials & Interfaces*, 2019, **11**, 14463-14477.
17. S. Ohta, T. Kobayashi and T. Asaoka, *Journal of Power Sources*, 2011, **196**, 3342-3345.
18. E. Rangasamy, J. Wolfenstine and J. Sakamoto, *Solid State Ionics*, 2012, **206**, 28-32.
19. S. Ohta, T. Kobayashi, J. Seki and T. Asaoka, *Journal of Power Sources*, 2012, **202**, 332-335.
20. Y. Li, J.-T. Han, C.-A. Wang, H. Xie and J. B. Goodenough, *Journal of Materials Chemistry*, 2012, **22**, 15357-15361.
21. Y.-T. Wang and X. Chen, *Tungsten*, 2022, **4**, 263-268.
22. C. Wang, K. Fu, S. P. Kammampata, D. W. McOwen, A. J. Samson, L. Zhang, G. T. Hitz, A. M. Nolan, E. D. Wachsman, Y. Mo, V. Thangadurai and L. Hu, *Chemical Reviews*, 2020, **120**, 4257-4300.
23. L. Xu, J. Li, W. Deng, H. Shuai, S. Li, Z. Xu, J. Li, H. Hou, H. Peng, G. Zou and X. Ji, *Advanced Energy Materials*, 2021, **11**, 2000648.
24. Z. Cheng, B. Zahiri, X. Ji, C. Chen, D. Chalise, P. V. Braun and D. G. Cahill, *Small*, 2021, **17**, 2101693.
25. J. Neises, W. S. Scheld, A.-R. Seok, S. Lobe, M. Finsterbusch, S. Uhlenbruck, R. Schmechel and N. Benson, *Journal of Materials Chemistry A*, 2022, **10**, 12177-12186.
26. Y. Zhou, C. Li, P. Koirala, G. A. Gamage, H. Wu, S. Li, N. K. Ravichandran, H. Lee, A. Dolocan, B. Lv, D. Broido, Z. Ren and L. Shi, *Physical Review Materials*, 2022, **6**, L061601.
27. A. A. Hubaud, D. J. Schroeder, B. J. Ingram, J. S. Okasinski and J. T. Vaughey, *Journal of Alloys and Compounds*, 2015, **644**, 804-807.
28. J. Y. Cho, X. Shi, J. R. Salvador, G. P. Meisner, J. Yang, H. Wang, A. A. Wereszczak, X. Zhou and C. Uher, *Physical Review B*, 2011, **84**, 085207.
29. C. Galven, J.-L. Fourquet, M.-P. Crosnier-Lopez and F. Le Berre, *Chemistry of Materials*, 2011, **23**, 1892-1900.
30. Y. Jin and P. J. McGinn, *Journal of Power Sources*, 2013, **239**, 326-331.
31. Y. Wang and W. Lai, *Journal of Power Sources*, 2015, **275**, 612-620.
32. H. Duan, H. Zheng, Y. Zhou, B. Xu and H. Liu, *Solid State Ionics*, 2018, **318**, 45-53.
33. W. Xia, B. Xu, H. Duan, X. Tang, Y. Guo, H. Kang, H. Li and H. Liu, *Journal of the American Ceramic Society*, 2017, **100**, 2832-2839.
34. Y. Li, A. M. Prabhu, T. S. Choksi and P. Canepa, *Journal of Materials Chemistry A*, 2022, **10**, 4960-4973.
35. L. Cheng, E. J. Crumlin, W. Chen, R. Qiao, H. Hou, S. Franz Lux, V. Zorba, R. Russo, R. Kostecki, Z. Liu, K. Persson, W. Yang, J. Cabana, T. Richardson, G. Chen and M. Doeff, *Physical Chemistry Chemical Physics*, 2014, **16**, 18294-18300.
36. A. Sharafi, S. Yu, M. Naguib, M. Lee, C. Ma, H. M. Meyer, J. Nanda, M. Chi, D. J. Siegel and J. Sakamoto, *Journal of Materials Chemistry A*, 2017, **5**, 13475-13487.

37. S. Yu, R. D. Schmidt, R. Garcia-Mendez, E. Herbert, N. J. Dudney, J. B. Wolfenstine, J. Sakamoto and D. J. Siegel, *Chemistry of Materials*, 2016, **28**, 197-206.
38. N. Hamao, K. Kataoka, N. Kijima and J. Akimoto, *Journal of the Ceramic Society of Japan*, 2016, **124**, 678-683.
39. K. Kataoka and J. Akimoto, *Journal of the Ceramic Society of Japan*, 2019, **127**, 521-526.
40. S. Adams and R. P. Rao, *Journal of Materials Chemistry*, 2012, **22**, 1426-1434.
41. T. Thompson, J. Wolfenstine, J. L. Allen, M. Johannes, A. Huq, I. N. David and J. Sakamoto, *Journal of Materials Chemistry A*, 2014, **2**, 13431-13436.
42. X. Chen, S. N. Girard, F. Meng, E. Lara-Curzio, S. Jin, J. B. Goodenough, J. Zhou and L. Shi, *Advanced Energy Materials*, 2014, **4**, 1400452.
43. B. Smith, G. Fleming, K. D. Parrish, F. Wen, E. Fleming, K. Jarvis, E. Tutuc, A. J. H. McGaughey and L. Shi, *Nano Letters*, 2020, **20**, 8384-8391.
44. M. Takashiri, S. Tanaka, H. Hagino and K. Miyazaki, *Journal of Applied Physics*, 2012, **112,** 084315.
45. S. Li, S. Guo, Y. Xu, J. Zhou and X. Chen, *ACS Applied Electronic Materials*, 2022, **4**, 787-794.
46. D. S. Smith, A. Alzina, J. Bourret, B. Nait-Ali, F. Pennec, N. Tessier-Doyen, K. Otsu, H. Matsubara, P. Elser and U. T. Gonzenbach, *Journal of Materials Research*, 2013, **28**, 2260-2272.
47. S. Guo, H. Li, X. Bai, Y. Wang, S. Li, R. E. Dunin-Borkowski, J. Zhou and X. Chen, *Cell Reports Physical Science*, 2024, **5,** 101879.
48. D. G. Cahill, S. K. Watson and R. O. Pohl, *Physical Review B*, 1992, **46**, 6131-6140.
49. X. Chen, A. Weathers, A. Moore, J. Zhou and L. Shi, *Journal of Electronic Materials*, 2012, **41**, 1564-1572.
50. G. J. Redhammer, M. Meven, S. Ganschow, G. Tippelt and D. Rettenwander, *Acta Crystallographica Section B*, 2021, **77**, 123-130.
51. X. Chen, C. Li, F. Tian, G. A. Gamage, S. Sullivan, J. Zhou, D. Broido, Z. Ren and L. Shi, *Physical Review Applied*, 2019, **11**, 064070.
52. S. Geller, G. P. Espinosa, L. D. Fullmer and P. B. Crandall, *Materials Research Bulletin*, 1972, **7**, 1219-1224.
53. N. L. Vočadlo and G. D. Price, *Physics of the Earth and Planetary Interiors*, 1994, **82**, 261-270.
54. C. L. Choy, *Journal of Polymer Science: Polymer Physics Edition*, 1975, **13**, 1263-1267.
55. E. Hirose, K. Niwa, K. Kataoka, J. Akimoto and M. Hasegawa, *Materials Research Bulletin*, 2018, **107**, 361-365.
56. S. Strangmüller, M. Avdeev, V. Baran, P. Walke, A. Kirchberger, T. Nilges and A. Senyshyn, *Zeitschrift für Naturforschung B*, 2022, **77**, 453-462.
57. Y. He, T. Day, T. Zhang, H. Liu, X. Shi, L. Chen and G. J. Snyder, *Advanced Materials*, 2014, **26**, 3974-3978.
58. D. A. Weber, A. Senyshyn, K. S. Weldert, S. Wenzel, W. Zhang, R. Kaiser, S. Berendts, J. Janek and W. G. Zeier, *Chemistry of Materials*, 2016, **28**, 5905-5915.
59. M. K. Gupta, J. Ding, D. Bansal, D. L. Abernathy, G. Ehlers, N. C. Osti, W. G. Zeier and O. Delaire, *Advanced Energy Materials*, 2022, **12**, 2200596.
60. Q. Ren, M. K. Gupta, M. Jin, J. Ding, J. Wu, Z. Chen, S. Lin, O. Fabelo, J. A. Rodríguez-Velamazán, M. Kofu, K. Nakajima, M. Wolf, F. Zhu, J. Wang, Z. Cheng, G. Wang, X. Tong, Y. Pei, O. Delaire and J. Ma, *Nature Materials*, 2023, **22**, 999-1006.
61. Z. F. Yow, Y. L. Oh, W. Gu, R. P. Rao and S. Adams, *Solid State Ionics*, 2016, **292**, 122-129.
62. H. Huo, Y. Chen, N. Zhao, X. Lin, J. Luo, X. Yang, Y. Liu, X. Guo and X. Sun, *Nano Energy*, 2019, **61**, 119-125.
63. Y. Li, X. Chen, A. Dolocan, Z. Cui, S. Xin, L. Xue, H. Xu, K. Park and J. B. Goodenough, *Journal of the American Chemical Society*, 2018, **140**, 6448-6455.
64. P. Pasierb, S. Komornicki, M. Rokita and M. Rękas, *Journal of Molecular Structure*, 2001, **596**, 151-156.

65. M. Nakayama, T. Horie, R. Natsume, S. Hashimura, N. Tanibata, H. Takeda, H. Maeda and M. Kotobuki, *The Journal of Physical Chemistry C*, 2023, **127**, 7595-7601.
66. Y.-N. Yang, Y.-X. Li, Y.-Q. Li and T. Zhang, *Nature Communications*, 2020, **11**, 5519.
67. Z. Liang and H.-L. Tsai, *International Journal of Heat and Mass Transfer*, 2012, **55**, 2999-3007.
68. M. Malakoutian, D. E. Field, N. J. Hines, S. Pasayat, S. Graham, M. Kuball and S. Chowdhury, *ACS Applied Materials & Interfaces*, 2021, **13**, 60553-60560.
69. C.-W. Nan and R. Birringer, *Physical Review B*, 1998, **57**, 8264-8268.

The data that support the findings of this study are available from the corresponding author upon reasonable request.